J. Fluid Mech. (2008), vol. 602, pp. 383–401. © 2008 Cambridge University Press
doi:10.1017/S002211200800102X Printed in the United Kingdom

Transverse-jet shear-layer instabilities. Part 2. Linear analysis for large jet-to-crossflow velocity ratio

LEONARDO S. DE B. ALVES[1], ROBERT E. KELLY[2] AND ANN R. KARAGOZIAN[2]

[1]Departamento de Engenharia Mecanica e de Materiais, IME, Rio de Janeiro, Brazil

[2]Department of Mechanical and Aerospace Engineering, University of California, Los Angeles,
Los Angeles, CA 90095-1597, USA

(Received 12 September 2006 and in revised form 8 February 2008)

The dominant non-dimensional parameter for isodensity transverse jet flow is the mean jet-to-crossflow velocity ratio, R. In Part 1 (Megerian *et al.*, *J. Fluid Mech.*, vol. 593, 2007, p. 93), experimental results are presented for the behaviour of transverse-jet near-field shear-layer instabilities for velocity ratios in the range $1 < R \leqslant 10$. A local linear stability analysis is presented in this paper for the subrange $R > 4$, using two different base flows for the transverse jet. The first analysis assumes the flow field to be described by a modified version of the potential flow solution of Coelho & Hunt (*J. Fluid Mech.*, vol. 200, 1989, p. 95), in which the jet is enclosed by a vortex sheet. The second analysis assumes a continuous velocity model based on the same inviscid base flow; this analysis is valid for the larger values of Strouhal number expected to be typical of the most unstable disturbances, and allows prediction of a maximum spatial growth rate for the disturbances. In both approaches, results are obtained by expanding in inverse powers of R so that the free-jet results are obtained as $R \to \infty$. The results from both approaches agree in the moderately low-frequency regime. Maximum spatial growth rates and associated Strouhal numbers extracted from the second approach both increase with decreasing velocity ratio R, in agreement with the experimental results from Part 1 in the range $4 < R \leqslant 10$. The nominally axisymmetric mode is found to be the most unstable mode in the transverse-jet shear-layer near-field region, upstream of the end of the potential core. The overall agreement of theoretical and experimental results suggests that convective instability occurs in the transverse-jet shear layer for jet-to-crossflow velocity ratios above 4, and that the instability is strengthened as R is decreased.

1. Introduction

The transverse jet or jet in crossflow is a canonical flow field that has widespread applications in engineering systems. Transverse jets involve the complex interaction of a round free jet with a perpendicular crossflow (see figure 1), generating a variety of different vortical structures, including near-field shear layer vortices. These near-field vortices, which arise due to shear-layer instabilities, undergo deformations that are thought (Kelso, Lim & Perry 1996; Cortelezzi & Karagozian 2001) to be associated with the formation of the well-known counter-rotating vortex pair or CVP, a flow structure associated with enhanced mixing by the transverse jet in comparison with that by the free jet.

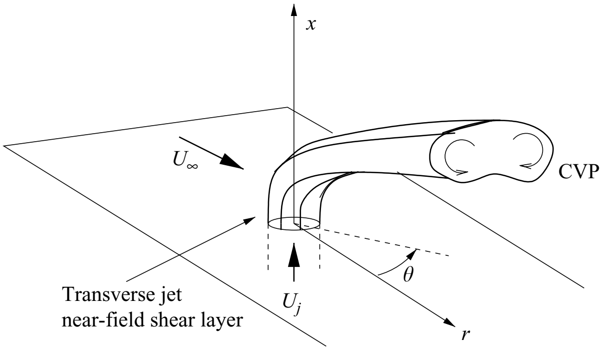

FIGURE 1. Schematic of the basic features of the jet in crossflow, including the counter-rotating vortex pair (CVP). The coordinate system for the present analysis is shown.

In Part 1 of the present paper (Megerian *et al.* 2007), the results of an extensive experimental investigation of the near-field shear-layer instabilities of an isodensity transverse jet are presented in terms of the jet-to-crossflow velocity ratio R as well as the jet Reynolds number $Re \equiv U_j D/\nu$ ($\geqslant$2000). For the larger values of R (typically $R > 4$), the instabilities are clearly observed to be convective in nature. The instabilities are strongly affected even by low-level jet forcing and tend to evolve spatially downstream, along the transverse-jet upstream shear layer. The growth rates of the dominant disturbances as well as their characteristic frequencies also increase as R decreases in this flow regime. However, for $R \lesssim 3.5$, the character of the instability changes and tends to become much stronger and more global in nature.

The present analysis is focused on the range $R > 4$ and hence pertains to an exploration of the convectively unstable flow. A linear local stability analysis is carried out by expanding in inverse powers of R or, for simplicity, in powers of $\lambda \equiv R^{-1}$. Thus, as $\lambda \rightarrow 0$ ($R \rightarrow \infty$), the established stability results for a free jet (as described, for instance, in the survey paper by Michalke 1984) are retrieved and serve as a basis of reference for the transverse jet. It is of interest to investigate how such results are influenced by a crossflow as well as to obtain results that can be compared to and assist in interpreting the experimental results of Part 1.

In order to carry out a stability analysis, a base flow for the transverse jet needs to be defined. No steady exact solution to the Navier–Stokes equations exists for this three-dimensional flow field. We make use of a modified version of the inviscid three-dimensional model for the near-field of a strong jet in crossflow developed by Coelho & Hunt (1989). Their solution is also obtained by expanding in powers of λ and so can be used on a consistent basis in the stability analysis. However, in the Coelho & Hunt (1989) solution, a vortex sheet encloses the jet, thereby leading to discontinuities in the axial and circumferential velocity components. For a free jet, such discontinuities give rise to growth rates that increase indefinitely with frequency for a spatial instability. In order to obtain a finite value of maximum growth rate, continuous velocity profiles are required. To achieve this, in the present paper we use modelling similar to that used for the free jet (see Michalke 1984).

In a separate paper by de B. Alves, Kelly & Karagozian (2007), the linear stability problem using the original inviscid solution of Coelho & Hunt (1989) as a base flow is investigated by means of a Fourier expansion in the circumferential direction, rather than an expansion in terms of λ. Growth rates are found to increase as λ increases, consistent with experimental observations (Part 1), but a maximum growth rate cannot be determined owing to the discontinuous base flow model. Also, numerical results in this prior study are restricted to the range $\lambda < 0.1$.

It should be mentioned that Blossey & Schmid (2002) (also discussed in Schmid 2007) report some results on a global stability analysis for the transverse jet that uses a time-averaged direct numerical simulation (DNS) of the flow field to determine a base flow without the temporal rollup of the shear layer. For the single case these authors explored, $\lambda = 1/6$, the stability analysis yields growth rates of the transverse-jet shear-layer modes that are found to be greater than for the case of a free jet. In the present study we use a simpler continuous base flow model to obtain linear stability analysis (LSA) results for a range of values of $\lambda < 1/4$, which enables exploration of the influence of a successively increasing crossflow magnitude on the stability.

2. The base flow

For a free jet with a thin initial shear layer, several modes have virtually the same growth rate close to the jet exit, as discussed for instance by Cohen & Wygnanski (1987). At about one diameter downstream, the axisymmetric mode obtains the largest growth rate, but the growth rate of the first helical mode then increases relative to the axisymmetric mode and that mode becomes dominant by three diameters downstream. The first helical mode is therefore dominant by the end of the potential core of the free jet (see also Yoda, Hesselink & Mungal 1992; Raman, Rice & Reshotko 1994). We will investigate how this modal development is affected by the crossflow in the region up to two diameters downstream for the transverse jet.

The starting point in determination of a suitable base flow for the transverse jet consists of the continuity equation in cylindrical coordinates for constant-density flow, namely,

$$\nabla \cdot \boldsymbol{u} = \frac{\partial u}{\partial x} + \frac{1}{r}\frac{1}{\partial r}(rv) + \frac{1}{r}\frac{\partial w}{\partial \theta} = 0, \tag{2.1}$$

where (u, v, w) are the velocity components in the x (along the jet), r (radial) and θ (circumferential) directions, respectively (see coordinates shown in figure 1), as well as the Euler equations,

$$\frac{\partial \boldsymbol{u}}{\partial t} + (\boldsymbol{u} \cdot \nabla)\boldsymbol{u} = -\nabla p. \tag{2.2}$$

All quantities have been made non-dimensional on the basis of the jet exit radius R_0, jet velocity U_j and ambient density ρ_0.

Coelho & Hunt (1989) obtain an inviscid solution for the basic flow of the transverse jet by expanding in terms of the parameter $\lambda \equiv U_\infty / U_j$ (where U_∞ is the free-stream velocity of the crossflow) and assuming the jet to be enclosed by a vortex sheet. As explained in de B. Alves *et al.* (2007), their solution for the velocity potentials ϕ_j in the jet and ϕ_e external to the jet can be expressed approximately as

$$\phi_j(x, r, \theta) = x + \lambda^2 (C_2 - x) r^2 \cos 2\theta + O(\lambda^3), \quad r < R_j \tag{2.3}$$

and

$$\phi_e(x, r, \theta) = \lambda \left(r + \frac{1}{r} \right) \cos\theta - \lambda^2 \left(\frac{C_2 - x}{r^2} \right) \cos 2\theta + O(\lambda^3), \quad r > R_j \tag{2.4}$$

where $\boldsymbol{u} = \nabla\phi$ and

$$R_j = 1 - \lambda^2 \{ x(x - 2C_2) + C_3 \} \cos 2\theta + O(\lambda^4) \tag{2.5}$$

represents the distortion of the circular jet that exists as $\lambda \to 0$. Note that for this solution to hold we need not only $\lambda \ll 1$ but also $(\lambda x) \ll 1$. This form of the solution ignores certain boundary effect terms that decay exponentially as x increases from the jet exit ($x = 0$). The numerical constants C_2 and C_3 arise from matching conditions imposed at $x = 0$. The first term in (2.4) corresponds to flow past a circular cylinder, whereas the second term, as discussed in de B. Alves *et al.* (2007), arises from matching via the kinematic condition and is a correction to the Coelho & Hunt (1989) solution.

Because ϕ_j and ϕ_e are potential flow solutions, the corresponding velocity components in the axial and circumferential directions are discontinuous at the jet boundary (as indicated by the vertical solid lines in the velocity profile plots in figure 2, discussed further below). As noted in § 1, discontinuous velocity profiles tend to give misleading stability results at large frequencies in comparison to results using continuous profiles. An attempt to obtain a uniformly valid solution by assuming a thin viscous region at the boundary of the jet is reported in the thesis of de B. Alves (2006). However, this analysis was not carried out successfully at $O(\lambda^2)$ and so cannot be used in general for the stability analysis. Hence, modelling in the manner of Michalke (1984) for the free jet is used for the transverse-jet base flow, even though neither theoretical nor local experimental results for the basic flow exist, and so cannot be used for comparison here.

It is assumed that the crossflow does not separate from the jet, which is consistent with the experimental observations of Fric & Roshko (1994). Also, in accordance with the assumption of inviscid flow, the effects of the horseshoe vortices that encompass the jet near its exit, and which arise from boundary layer separation, are ignored. These vortices cause the streamlines of the flow only to dip somewhat upstream of the jet, as documented by Kelso & Smits (1995) for the range of R considered in this paper. At lowest order, the flow in the x-direction near $r = 1$ is assumed to be represented by the hyperbolic tangent velocity profile (corresponding to profile No. 2 of Michalke 1984)

$$\hat{U}_0(r;\theta_0) = \frac{1}{2} - \frac{1}{2}\tanh\left\{\frac{1}{4\theta_0}\left(r - \frac{1}{r}\right)\right\} \tag{2.6}$$

where the local non-dimensional momentum thickness θ_0 depends on the downstream distance x generally in the manner proposed by Crighton & Gaster (1976) for a free jet, namely,

$$\theta_0(x) = \frac{3x+4}{100} \quad \text{or} \quad x = \frac{4}{3}(25\theta_0 - 1). \tag{2.7}$$

The profile given by (2.6) tends to unity as $r \to 0$ and to zero as $r \to \infty$. As shown by the results in Michalke (1984), this profile is in reasonable agreement with the experimentally measured profile for the free jet up to the end of the potential core.

Denoting basic flow quantities by capital letters, we now define the base flow velocity components in terms of λ as

$$U(r,\theta;\theta_0) = \hat{U}_0(r;\theta_0) + \lambda^2 U_2(r,\theta;\theta_0), \tag{2.8}$$

$$V(r,\theta;\theta_0) = \lambda V_1(r,\theta;\theta_0) + \lambda^2 V_2(r,\theta;\theta_0), \tag{2.9}$$

$$W(r,\theta;\theta_0) = \lambda W_1(r,\theta;\theta_0) + \lambda^2 W_2(r,\theta;\theta_0). \tag{2.10}$$

We truncate the expressions at $O(\lambda^2)$ because we will later be determining only an $O(\lambda^2)$ correction to the growth rates. Outside the shear layers, U, V, and W must match the velocities associated with the flow described in equations (2.3) and (2.4) as

$r \to 1$. Hence we further define

$$U_2(r,\theta;\theta_0) = \hat{U}_2(r;\theta_0)\cos 2\theta, \tag{2.11}$$

$$V_1(r,\theta;\theta_0) = \hat{V}_1(r;\theta_0)\cos\theta, \quad V_2(r,\theta;\theta_0) = \hat{V}_2(r;\theta_0)\cos 2\theta, \tag{2.12}$$

$$W_1(r,\theta;\theta_0) = -\hat{W}_1(r;\theta_0)\sin\theta, \quad W_2(r,\theta;\theta_0) = -\hat{W}_2(r;\theta_0)\sin 2\theta. \tag{2.13}$$

Making further use of the function defined by (2.6), we write

$$\hat{U}_2 = -r^2\hat{U}_0 + \left(\frac{1-\hat{U}_0}{r^2}\right), \quad \hat{W}_1 = \left(1+\frac{1}{r^2}\right)(1-\hat{U}_o). \tag{2.14}$$

The function $\hat{V}_1$ is determined by use of the continuity equation in order to conserve mass. The reader is referred to de B. Alves (2006) for the corresponding expressions for $\hat{V}_1$, $\hat{V}_2$, and $\hat{W}_2$, which are developed in an analogous manner. The radial behaviour of the different functions comprising the base flow is shown for various values of the local inverse momentum thickness $(\theta_0)^{-1}$ in figure 2, along with the irrotational profiles (solid lines). The results seem to be reasonable in creating a continuous base flow, but it should be emphasized that the functions are ad hoc, and are not to be interpreted as exact solutions of the momentum conservation equations for the full three-dimensional transverse jet flow field.

3. Linear stability analysis

The linear stability analysis of the irrotational flow (based on (2.3) and (2.4)) using a multiple mode approach via Fourier expansions is described in de B. Alves *et al.* (2007). A linearized analysis of the same base flow via a perturbation expansion approach in λ will be described briefly in § 3.1. This alternative approach allows a better understanding of the influence of subharmonic resonances on transverse jet stability characteristics and determination of growth rates for a wide range of λ.

The bulk of this section will focus on an analysis of the stability of the continuous base flow ((2.8)–(2.10)). The change in growth rate for the irrotational case is obtained by solving for the flow within and outside the jet and then matching the solutions at $r = R_j(x,\theta)$. In contrast, for the case of continuous velocity profiles, the change in growth rate is obtained by means of a solvability condition involving an integral over the entire flow field. Yet some features are the same. Each analysis involves an expansion in terms of λ, and in addition, each solution is of a local nature so that the x-dependence of basic flow quantities is parameterized in terms of θ_0, just as in the stability analysis of the free jet (Michalke 1984). Owing to the complicated nature of the analysis, the equations have been derived and solved using the symbolic and numerical computation capabilities of the software *Mathematica* by Wolfram (1999).

3.1. *Irrotational flow analysis*

The governing equations, interfacial kinematic conditions, and linearization and normal mode analysis for the irrotational base flow ((2.3) and (2.4)) are the same as explained in de B. Alves *et al.* (2007), see § 3.1 and § 3.2 of that paper for details. Coelho & Hunt's modified solution ((2.3) and (2.4)) is perturbed by introducing infinitesimal disturbances not only for the velocity potential but for the interface displacement as well. Because the free jet is sensitive to disturbances that undergo convective instability (see Huerre & Monkewitz 1990), we expect the same to be true for the transverse jet, at least for small values of λ. We therefore assume that these disturbances evolve spatially. Here, the overall velocity potential within and exterior

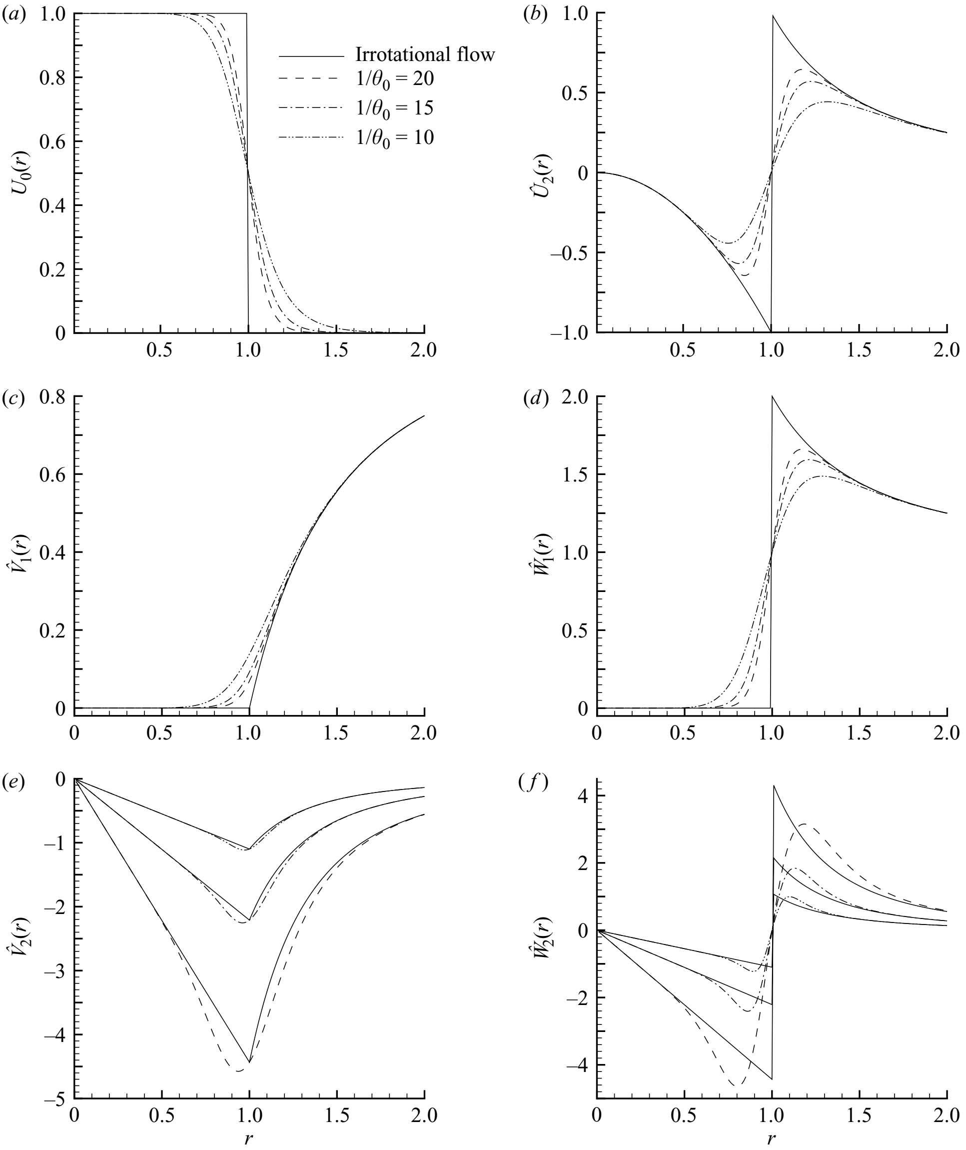

FIGURE 2. Radial behaviour of tanh and irrotational base flow components: (*a*) $\widehat{U}_0(r)$, (*b*) $\widehat{U}_2(r)$, (*c*) $\widehat{V}_1(r)$, (*d*) $\widehat{W}_1(r)$, (*e*) $\widehat{V}_2(r)$ and (*f*) $\widehat{W}_2(r)$.

to the jet (called ϕ_j^* and ϕ_e^*, respectively) and the distorted jet interface may be written in terms of mean and perturbation quantities, the latter of which can be separated into Fourier modes:

$$\phi_j^* \equiv \phi_j + \widetilde{\phi}_j = \phi_j + \Phi_j(r,\theta)\ \exp[\mathrm{i}\,(\alpha\, x - \omega\, t)], \tag{3.1a}$$

$$\phi_e^* \equiv \phi_e + \widetilde{\phi}_e = \phi_e + \Phi_e(r,\theta)\ \exp[\mathrm{i}\,(\alpha\, x - \omega\, t)], \tag{3.1b}$$

$$R_j^* \equiv R_j + \widetilde{R}_j = R_j + \mathscr{N}(\theta)\ \exp[\mathrm{i}\,(\alpha\, x - \omega\, t)], \tag{3.1c}$$

with $\mathrm{i} \equiv \sqrt{-1}$, and ϕ_j, ϕ_e and R_j given by relations (2.3), (2.4) and (2.5). Since we assume that disturbances grow spatially, the wavenumber α is taken to be a complex number and the frequency ω is an arbitrary real number. A local stability analysis is performed in this study, so that $x = x_0$ becomes a parameter in our analysis at $O(\lambda^2)$, and thus $\theta_0 = \theta_0(x_0)$. Substituting relations (3.1) into the continuity equation interior and exterior to the transverse jet yields partial differential equations for ϕ_j and ϕ_e whose solutions are then matched. After linearizing the location of the disturbed interface, the kinematic and dynamic matching conditions are the same as those derived in de B. Alves *et al.* (2007).

The inviscid base flow described in §2 is accurate only up to $O(\lambda^2)$. We take advantage of λ being a small parameter and expand the disturbance variables in terms of λ as well, noting that when $\lambda = 0$ we recover the well-known free-jet dispersion relation obtained by Batchelor & Gill (1962). Thus, we have to $O(\lambda^2)$:

$$\varPhi_j = \varPhi^{+}_{j,0}(r)\,\exp[+\mathrm{i}\,m\,\theta] + \varPhi^{-}_{j,0}(r)\,\exp[-\mathrm{i}\,m\,\theta] + \lambda\,\varPhi_{j,1}(r,\theta) + \lambda^2\,\varPhi_{j,2}(r,\theta), \qquad (3.2a)$$

$$\varPhi_e = \varPhi^{+}_{e,0}(r)\,\exp[+\mathrm{i}\,m\,\theta] + \varPhi^{-}_{e,0}(r)\,\exp[-\mathrm{i}\,m\,\theta] + \lambda\,\varPhi_{e,1}(r,\theta) + \lambda^2\,\varPhi_{e,2}(r,\theta), \qquad (3.2b)$$

$$\mathscr{N} = \mathscr{N}^{+}_{0}\,\exp[+\mathrm{i}\,m\,\theta] + \mathscr{N}^{-}_{0}\,\exp[-\mathrm{i}\,m\,\theta] + \lambda\,\mathscr{N}_1(\theta) + \lambda^2\,\mathscr{N}_2(\theta), \qquad (3.2c)$$

$$\alpha = \alpha_0 + \lambda\,\alpha_1 + \lambda^2\,\alpha_2, \quad \omega = \omega_0. \qquad (3.2d,e)$$

We focus on a disturbance with a fixed frequency ω_0, consistent with the spatial stability analysis.

It is important to emphasize that although it is known that the lowest-order disturbances, i.e. the free-jet disturbances, are independent of the sign of the azimuthal mode number m, which appears only as m^2 in the governing equations, we must introduce disturbances of both signs at this order to allow a proper interaction of these disturbances with the crossflow. The + or − superscripts in equations (3.2) denote helical modes of different sense (counterclockwise and clockwise, respectively). This issue is relevant to the case of helical disturbances only, since for axisymmetric disturbances, $m = 0$ and there is no θ dependence at lowest order. For $m = 0$, the lowest-order disturbance quantities in relations (3.2) are simply $\varPhi_{j,0}(r)$, $\varPhi_{e,0}(r)$ and $\mathscr{N}_0$. Hence when we later refer to an ‘axisymmetric’ disturbance, we mean that the disturbance reduces to these values as $\lambda \to 0$.

A further approximation is also introduced. The kinematic and dynamic conditions must be evaluated at the transverse jet interface R_j, which depends on λ as shown in equation (2.5). Hence, we use a Taylor series expansion to approximate the location of the disturbed interface as

$$f(R_j,\theta;x_0) \simeq f(1,\theta;x_0) + \lambda^2\,R_{j,2}(x_0)\,\cos[2\,\theta]\,\left.\frac{\partial f}{\partial r}\right|_{r=1} + \cdots, \qquad (3.3)$$

where $R_{j,2}(x_0)$ represents the term within brackets in equation (2.5).

The present perturbation expansion approach enables us to obtain a relevant dispersion relation for the zeroth-order problem, that is, where only terms of order λ^0 are utilized. Following the analysis by Batchelor & Gill (1962) for the case of temporal instability, we obtain the zeroth-order dispersion relation

$$D^{(0)}_m = \left(\frac{\omega_0 - \alpha_0}{\omega_0}\right)^2 - \frac{I'_m(\alpha_0)\,K_m(\alpha_0)}{I_m(\alpha_0)\,K'_m(\alpha_0)} = 0, \qquad (3.4)$$

where I_m and K_m are modified Bessel functions. After selecting the integer azimuthal number m and the real frequency ω_0, we can then calculate the complex wavenumber

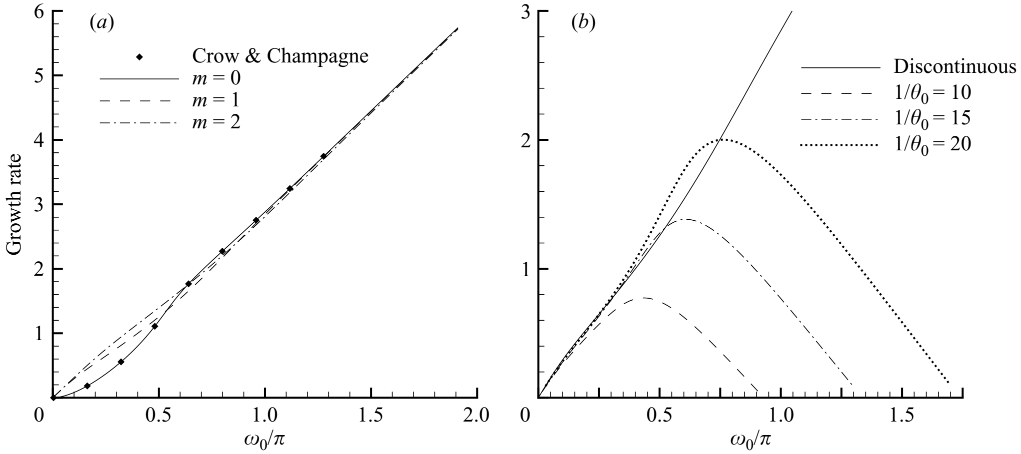

FIGURE 3. (*a*) Irrotational free-jet growth rate ($-\mathrm{Im}[\alpha_0]$) versus ω_0/π for azimuthal numbers $m = 0, 1$ and 2. Points are taken from Crow & Champagne (1971). (*b*) Free-jet first helical mode ($m = 1$) growth rate versus ω_0/π. Comparison between discontinuous (irrotational) and continuous (tanh function, from Michalke (1984)) base flows.

α_0 from this dispersion relation. The spatial growth rate curves for the free-jet axisymmetric mode ($m = 0$), as well as the first ($m = 1$) and second ($m = 2$) helical modes, are shown in figure 3(*a*), along with results from the earlier spatial analysis of Crow & Champagne (1971) for the free jet. Note that the growth rate of the axisymmetric mode is the largest as long as $\omega_0/\pi > 0.6$, approximately.

The linear stability results obtained from an analysis of the discontinuous profile are in agreement with those obtained from the continuous profile for small frequencies, as will be discussed further in the next section. However, we note that the range in which both solutions agree depends on the thickness of the jet shear layer in the continuous profile. Figure 3(*b*) shows a comparison between free-jet growth rates for the first helical mode obtained from a continuous base flow and from the present discontinuous base flow. The continuous results are obtained using the same hyperbolic tangent function (2.6) for three different values of $1/\theta_0$, namely, 20, 15 and 10. One can see that as the local shear layer thickness decreases, i.e. as the momentum thickness decreases or θ_0^{-1} increases, the range in which both results agree widens.

Analyses of the nature of the disturbances at first order (λ^1) and second order (λ^2) are discussed in detail in de B. Alves (2006). Although there is no correction arising from the introduction of crossflow to the first-order wavenumber ($\alpha_1 = 0$), the order-λ^1 disturbances are still non-zero in general. An important exception is the case of axisymmetric disturbances, where we have $m = 0$ and the constants in the solution are zero, because they are found to be proportional to m. For this situation, the only $O(\lambda)$ term that could introduce the crossflow into the solution is the term involving $\partial\phi_e/\partial r$ in the dynamic condition at the deformed jet interface, but this term is zero at the linearized interface $r = 1$. Moreover, the first-order solution suggests that for the first and second helical modes ($m = 1$ and $m = 2$), the solution is ill-defined in the small-frequency limit because the growth rates for these two modes approach each other in this limit, leading to singular behaviour.

At second order in λ, as described in de B. Alves (2006), there is no $O(\lambda^2)$ correction to the growth rate for $m = 0$ because the $O(\lambda)$ solution is zero. Also, one observes

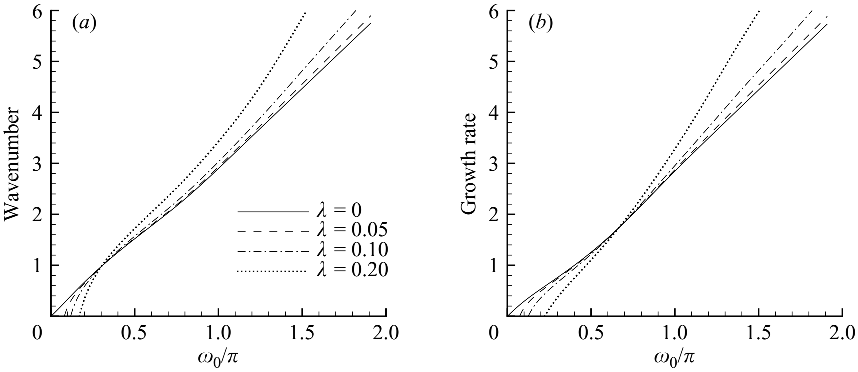

FIGURE 4. First helical mode for discontinuous base flow model: (*a*) wavenumber (Re [α]) and (*b*) growth rate (−Im [α]) vs ω_0/π at velocity ratios $\lambda = 0$, 0.05, 0.1 and 0.2, at $x_0 = 1$.

a subharmonic resonance (when $m = \pm 1$) which is akin to that studied by Corke & Kusek (1993) for a cylindrical shear layer between an axisymmetric mode ($m = 0$) and two forced helical modes ($m = \pm 1$) with half the frequency. However, in the present case, one agent involved in the subharmonic resonance is a steady component of the transverse jet's base flow proportional to $\cos 2\theta$, and the resonance arises due to azimuthal interactions between it and the fundamental modes when $m = \pm 1$. Owing to the interaction, non-homogeneous terms arise that resonate with the fundamental modes. For this reason, we examine the two cases $m \neq 1$ and $m = 1$ separately, which produces two different solvability conditions. Because for $m = \pm 1$ the resonating term has twice the period in θ as the steady flow term that acts as a forcing, we refer to the response as being a subharmonic.

As in the first-order analysis, for the second-order analysis (of order λ^2), we find that the ill-defined nature of the perturbation expansion solution for the first helical mode ($m = 1$) renders the result for low frequency, $\omega_0/\pi < 0.2$, unreliable. At higher Strouhal numbers we observe that increasing the crossflow velocity (i.e. increasing λ from zero) generally increases the growth rate of the first helical mode. The total wavenumber and growth rate for this mode are shown in figure 4 as functions of the Strouhal number for different values of λ, at the location $x_0 = 1$. It should be mentioned that separate calculations of the growth rate of the first helical mode were also done in de B. Alves (2006) on the basis that the jet cross-section remains cylindrical (i.e. $R_j = 1$ rather than the expression in (2.5)). The results in this instance are almost identical to those shown in figure 4 with the deformed jet boundary.

In order to determine the impact of the subharmonic resonance on the first helical mode wavenumber and growth rate, these parameters were also recalculated without the extra terms that appear in the analysis due to this special interaction. The corresponding results are shown in figure 5, which shows the total wavenumber and growth rate for this mode as functions of frequency for different values of λ at $x_0 = 1$, with the free-jet result ($\lambda = 0$) shown for reference. Although the wavenumber correction with and without the subharmonic resonance varies little, so that figures 4(*a*) and 5(*a*) differ only slightly, the absence of this special interaction increases the frequency at which the switch occurs by about 25 % for the growth rate correction (cf. figures 4*b* and 5*b*). Hence, the subharmonic resonance itself effectively increases the destabilization brought about by the crossflow.

The corrections to the second helical mode are obtained similarly to those for the first helical mode described above. As with the first helical mode corrections, both

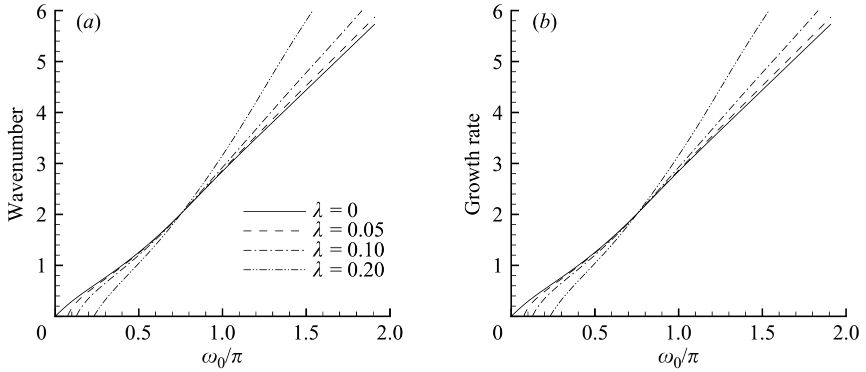

FIGURE 5. As figure 4, but calculated without the additional resonant terms.

wavenumber and growth rate corrections are negative at low frequencies but positive at high frequencies, although the switch occurs at somewhat higher frequencies. Details on these results may be found in de B. Alves (2006).

3.2. *Analysis of flow with continuous velocity profiles*

We now perform a linear stability analysis using the continuous base flow quantities to $O(\lambda^2)$ defined in (2.6)–(2.14) and use directly the continuity and momentum conservation equations (2.1) and (2.2). The LSA for the continuous base flow is valid for the larger values of Strouhal number expected to be typical of the most unstable disturbances.

For the stability analysis, we set

$$\boldsymbol{u}(\boldsymbol{x}, t) = \boldsymbol{U}(\boldsymbol{x}) + \boldsymbol{u}'(\boldsymbol{x}, t), \tag{3.5}$$

$$p(\boldsymbol{x}, t) = \bar{P}(\boldsymbol{x}) + p'(\boldsymbol{x}, t). \tag{3.6}$$

Substituting into (2.1), (2.2), we obtain

$$\nabla \boldsymbol{\cdot} \boldsymbol{u}' = \frac{\partial u'}{\partial x} + \frac{1}{r}\frac{\partial}{\partial r}(rv') + \frac{1}{r}\frac{\partial w'}{\partial \theta} = 0 \tag{3.7}$$

and

$$\frac{\partial \boldsymbol{u}'}{\partial t} + (\boldsymbol{U} \boldsymbol{\cdot} \nabla)\boldsymbol{u}' + (\boldsymbol{u}' \boldsymbol{\cdot} \nabla)\boldsymbol{U} = -\nabla p'. \tag{3.8}$$

Although our representation of the base flow given in (3.5) and (3.6) is not an exact solution of the momentum equations, we assume that the approximations shown in figure 2 are adequate for studying the stability characteristics of the actual flow which presumably depend upon vorticity dynamics. We again perform a local stability analysis by further assuming that x has a fixed value x_0 as far as the basic flow quantities are concerned. Hence, $\theta_0(x) = \theta_0(x_0)$ in the following discussion. We also assume that the disturbances can be represented in a Fourier manner as

$$u' = F(r, \theta)e^{i(\alpha x - \omega t)} + \text{c.c.}, \quad v' = iG(r, \theta)e^{i(\alpha x - \omega t)} + \text{c.c.}, \tag{3.9}$$

$$w' = iH(r, \theta)e^{i(\alpha x - \omega t)} + \text{c.c.}, \quad p' = P(r, \theta)e^{i(\alpha x - \omega t)} + \text{c.c.}, \tag{3.10}$$

where the frequency ω is assumed to be real, the wavenumber α is taken to be complex, and c.c. denotes complex conjugate. After substituting (3.9) and (3.10) into

(3.7) and (3.8), we obtain

$$\alpha F + \frac{1}{r}\frac{\partial}{\partial r}(rG) + \frac{1}{r}\frac{\partial H}{\partial \theta} = 0, \tag{3.11}$$

$$-\mathrm{i}(\omega - \alpha U)F + \left(V\frac{\partial F}{\partial r} + \frac{W}{r}\frac{\partial F}{\partial \theta}\right) + \frac{\mathrm{i}}{r}\frac{\partial U}{\partial \theta}H + \mathrm{i}\frac{\partial U}{\partial r}G = -\mathrm{i}\alpha P, \tag{3.12}$$

$$\left(\omega - \alpha U + \mathrm{i}\frac{\partial V}{\partial r}\right)G + \mathrm{i}\left(V\frac{\partial G}{\partial r} + \frac{W}{r}\frac{\partial G}{\partial \theta}\right) + \mathrm{i}\left(\frac{1}{r}\frac{\partial V}{\partial \theta} - \frac{2W}{r}\right)H = -\frac{\partial P}{\partial r}, \tag{3.13}$$

$$\frac{\mathrm{i}}{r}\frac{\partial}{\partial r}(rW)G + \left(\omega - \alpha U + \mathrm{i}\left(\frac{V}{r} + \frac{1}{r}\frac{\partial W}{\partial \theta}\right)\right)H + \mathrm{i}\left(V\frac{\partial H}{\partial r} + \frac{W}{r}\frac{\partial H}{\partial \theta}\right) = -\frac{1}{r}\frac{\partial P}{\partial \theta}. \tag{3.14}$$

We now expand in terms of λ up to $O(\lambda^2)$, using the free-jet results at lowest order:

$$P(r,\theta) = {P_0}^{+}(r)\mathrm{e}^{\mathrm{i}m\theta} + {P_0}^{-}(r)\mathrm{e}^{-\mathrm{i}m\theta} + \lambda P_1(r,\theta) + \lambda^2 P_2(r,\theta), \tag{3.15}$$

$$F(r,\theta) = {F_0}^{+}(r)\mathrm{e}^{\mathrm{i}m\theta} + {F_0}^{-}(r)\mathrm{e}^{-\mathrm{i}m\theta} + \lambda F_1(r,\theta) + \lambda^2 F_2(r,\theta), \tag{3.16}$$

$$G(r,\theta) = {G_0}^{+}(r)\mathrm{e}^{\mathrm{i}m\theta} + {G_0}^{-}(r)\mathrm{e}^{-\mathrm{i}m\theta} + \lambda G_1(r,\theta) + \lambda^2 G_2(r,\theta), \tag{3.17}$$

$$H(r,\theta) = {H_0}^{+}(r)\mathrm{e}^{\mathrm{i}m\theta} + {H_0}^{-}(r)\mathrm{e}^{-\mathrm{i}m\theta} + \lambda H_1(r,\theta) + \lambda^2 H_2(r,\theta). \tag{3.18}$$

The azimuthal wavenumber m is equal to an integer, or is equal to zero for the nominally axisymmetric case. The wavenumber α is expanded in a similar manner as

$$\alpha = \alpha_0 + \lambda\alpha_1 + \lambda^2\alpha_2, \quad \omega = \omega_0. \tag{3.19}$$

Zeroth-order analysis: The free jet

The solution procedure was developed for an arbitrary value of m (see de B. Alves 2006), but in order to save space, we show the details for only the nominally axisymmetric case $m=0$, after defining the first two terms in (3.15) as $P_0(r)$, etc. After substitution into (3.11)–(3.14), the lowest-order terms can be combined into a single equation for $P_0(r)$, namely,

$$\frac{\mathrm{d}^2P_0}{\mathrm{d}r^2} + \left(\frac{1}{r} + \left(\frac{2\alpha_0}{\omega_0 - \omega_0 U_0}\frac{\mathrm{d}U_0}{\mathrm{d}r}\right)\right)\frac{\mathrm{d}P_0}{\mathrm{d}r} - {\alpha_0}^2 P_0 = 0 \tag{3.20}$$

to be solved subject to the boundary conditions

$$\lim_{r\to 0} P_0 \sim \text{finite}, \quad \lim_{r\to\infty} P_0 = 0. \tag{3.21}$$

Noting that $\mathrm{d}U_0/\mathrm{d}r \to 0$ as $r \to 0$ and $r \to \infty$, we can obtain the asymptotic solutions

$$P_0(r \ll 1) = c_1 I_0(\alpha_0 r), \quad P_0(r \gg 1) = c_2 K_0(\alpha_0 r), \tag{3.22}$$

where I_0 and K_0 denote the usual Bessel functions. The asymptotic solutions are used as initial conditions for the integration of (3.20) towards $r=1$, using an initial guess for α_0, and α_0 is then iterated upon until P_0 and P_0' are matched at that point. The results for wavenumber and growth rate are in agreement with earlier results for the free jet, e.g. Michalke (1984).

First-order analysis

At $O(\lambda)$, one can argue heurestically that the result should be independent of the sign of U_∞, i.e. the sign of λ, and therefore that $\omega_1 = \alpha_1 = 0$. The same result can be shown rigorously from the $O(\lambda)$ disturbance equations. Thus, the role of the $O(\lambda)$

equations is to give a correction to the lowest-order eigenfunctions. Examination of the non-homogenous terms in the $O(\lambda)$ equations suggests a solution with the form

$$P_1(r,\theta)=\hat{P}_1(r)\cos\theta,\quad F_1(r,\theta)=\hat{F}_1(r)\cos\theta, \tag{3.23}$$

$$G_1(r,\theta)=\hat{G}_1(r)\cos\theta,\quad H_1(r,\theta)=\hat{H}_1(r)\sin\theta. \tag{3.24}$$

The resulting equations can be reduced to the following equation for $\hat{P}_1(r)$:

$$\frac{\mathrm{d}^2\hat{P}_1}{\mathrm{d}r^2}+\left(\frac{1}{r}+\frac{2\alpha_0}{\omega_0-\alpha_0U_0}\frac{\mathrm{d}U_0}{\mathrm{d}r}\right)\frac{\mathrm{d}\hat{P}_1}{\mathrm{d}r}-\left({\alpha_0}^2+\frac{1}{r^2}\right)\hat{P}_1=\Lambda_1(r) \tag{3.25}$$

where

$$\Lambda_1(r)=-\left[\mathrm{i}\alpha_0\hat{V}_1\frac{\mathrm{d}F_0}{\mathrm{d}r}+\mathrm{i}\left(\frac{1}{r}+\frac{2\alpha_0}{\omega_0-\alpha_0U_0}\frac{\mathrm{d}U_0}{\mathrm{d}r}+\frac{\mathrm{d}}{\mathrm{d}r}\right)\frac{\mathrm{d}}{\mathrm{d}r}(\hat{V}_1G_0)+\frac{\mathrm{i}}{r^2}\frac{\mathrm{d}}{\mathrm{d}r}(r\hat{W}_1)G_0\right] \tag{3.26}$$

and where $\hat{P}_1(r)$ satisfies the same boundary conditions (3.21) as P_0. The homogenous form of (3.25) corresponds to the equation governing the first helical mode ($m=1$) but α_0 corresponds to the eigenvalue for the axisymmetric mode, and so there is no difficulty in obtaining a solution to (3.25). This is done numerically in a manner similar to that used for the solution of P_0, and the results are used in the $O(\lambda^2)$ problem, which yields the change in growth rate.

Second-order analysis

Continuing the above discussion, difficulties will arise in the $O(\lambda^2)$ problem if axisymmetric non-homogeneous terms arise, and a solution will be possible then only if a solvability condition involving α_2 is satisfied. Restricting our attention only to the axisymmetric part of the $O(\lambda^2)$ solution, say $\overline{P}_2(r)$, $\overline{F}_2(r)$, and $\overline{G}_2(r)$, since $\overline{H}_2$ can be shown to be zero, an equation for $\overline{P}_2(r)$ can be developed with the form

$$\frac{\mathrm{d}^2\bar{P}_2}{\mathrm{d}r^2}+\left(\frac{1}{r}+\frac{2\alpha_0}{\omega_0-\alpha_0U_0}\frac{\mathrm{d}U_0}{\mathrm{d}r}\right)\frac{\mathrm{d}\bar{P}_2}{\mathrm{d}r}-{\alpha_0}^2\bar{P}_2=\Gamma(r) \tag{3.27}$$

where

$$\begin{aligned}\Gamma&=\alpha_2\omega_0F_0+\alpha_0\alpha_2P_0+\frac{{\alpha_0}^2}{2}\hat{U}_1\hat{F}_1\\&\quad-\alpha_0\left\{\mathrm{i}\hat{V}_1\frac{\mathrm{d}\hat{F}_1}{\mathrm{d}r}+\frac{\mathrm{i}}{2r}\hat{W}_1\hat{F}_1-\frac{1}{2}\frac{\mathrm{d}\hat{U}_1}{\mathrm{d}r}\hat{G}_1+\frac{1}{2r}\hat{U}_1\hat{H}_1\right\}\\&\quad+\left(\frac{1}{r}+\frac{2\alpha_0}{\omega_0-\alpha_0U_0}\frac{\mathrm{d}U_0}{\mathrm{d}r}+\frac{\mathrm{d}}{\mathrm{d}r}\right)\left(\alpha_2U_0G_0+\frac{\alpha_0}{2}\hat{U}_1\hat{G}_1\right.\\&\quad\left.-\frac{\mathrm{i}}{2}\frac{\mathrm{d}}{\mathrm{d}r}(\hat{V}_1\hat{G}_1)+\frac{\mathrm{i}}{2r}\hat{W}_1\hat{G}_1+\frac{\mathrm{i}}{2r}(\hat{V}_1+2\hat{W}_1)\hat{H}_1\right).\end{aligned} \tag{3.28}$$

This equation, which has a homogenous solution P_0 that satisfies the boundary conditions, has a solution only if, once the equation is placed in self-adjoint form, the non-homogeneous terms are orthogonal to the homogeneous solution (i.e. the Fredholm alternative is satisfied). The solvability condition is then represented by

$$\int_0^\infty\frac{r\Gamma P_0\,\mathrm{d}r}{(\omega_0-\alpha_0U_0)^2}=0 \tag{3.29}$$

which allows us to solve for α_2 explicitly.

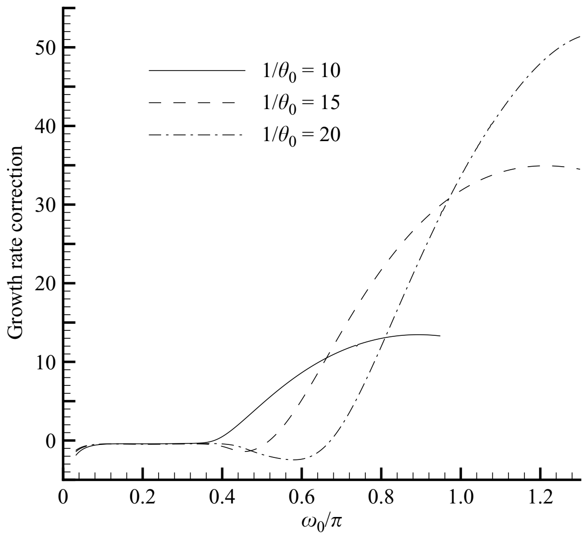

FIGURE 6. Axisymmetric mode growth rate correction ($-\text{Im}[\alpha_2]$) versus ω_0/π for tanh base flow model with $1/\theta_0 = 10$, 15 and 20.

The analysis for the helical modes is similar to the above, and is given in de B. Alves (2006). The main difference occurs for the first helical mode, where a subharmonic resonance can occur between the disturbance and the $O(\lambda^2)$ part of the base flow, similarly to that described in § 3.1 for the case of discontinuous profiles. This leads to additional terms at $O(\lambda^2)$ relative to the case $m \neq 1$. A discussion of the relevant results for the continuous base flow case is provided in the next section.

4. Results

As mentioned in § 1, in studies on the free jet, emphasis has typically been placed on discussion of the development of the axisymmetric mode ($m = 0$) and the first helical mode ($m = 1$). The higher helical modes ($m = 2, 3, \ldots$) tend to have distinctly lower growth rates in the downstream region; see figure 8 of Cohen & Wygnanski (1987), for example. We will do likewise in our discussion of the results for the transverse jet, although some results given in de B. Alves (2006) for the $m = 2$ mode will be mentioned in passing.

We begin our discussion by recalling, for the irrotational base flow analysis in § 3.1, that the $O(\lambda)$ problem indicates that first-order disturbances are zero when $m = 0$. Hence there is no correction to the growth rate of the axisymmetric mode for the irrotational base flow model up to $O(\lambda^2)$. This result no longer holds for the case of continuous velocity profiles at moderate frequencies, however, as demonstrated in the plots of axisymmetric growth rate correction as a function of frequency for different θ_0 and R values, shown in figures 6 and 7, respectively. The correction to the growth rate is very small at $\omega_0/\pi < 0.4$, as shown in figure 6; this is the range where the potential flow analysis is most relevant to the continuous flow case. Hence, the axisymmetric mode growth rate correction is deemed negligible up to a value of $\omega_0/\pi \cong 0.4$. For some $\omega_0/\pi > 0.4$, depending on the value of $(\theta_0)^{-1}$, the correction becomes positive, thus denoting destabilization, and increases to a maximum at some larger value of ω_0/π, again depending on $(\theta_0)^{-1}$. This trend tends to shift the maximum overall axisymmetric mode growth rate for decreasing values of $R = \lambda^{-1}$ to higher values of

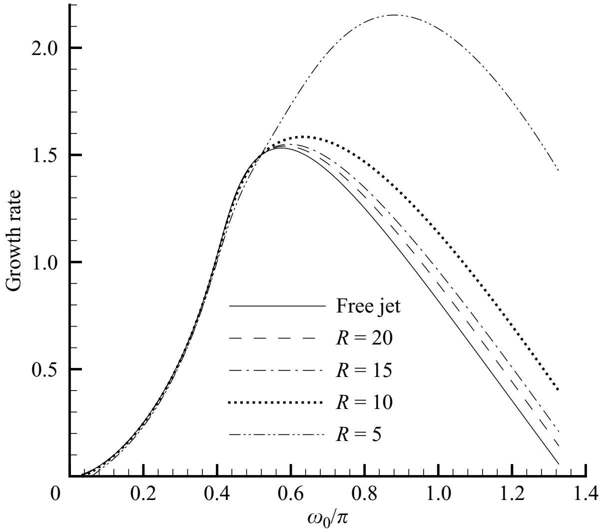

FIGURE 7. Axisymmetric mode growth rate ($-\text{Im}[\alpha]$) versus ω_0/π for tanh base flow model with $R = \infty$, 20, 15, 10 and 5, with $1/\theta_0 = 15$.

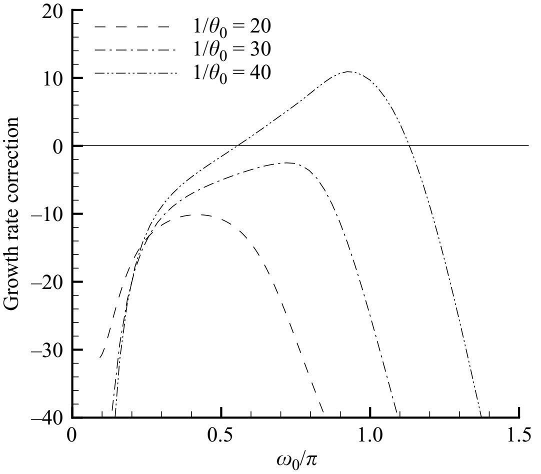

FIGURE 8. First helical mode growth rate correction versus ω_0/π from the tanh base flow model.

ω_0/π, as shown in figure 7 for a fixed value of $(\theta_0)^{-1}$. The predictions that the growth rate increases and that the maximum growth rate occurs at a higher value of ω_0/π as λ increases (or R decreases) agree with the experimental trends reported in Part 1. A direct comparison of experimental and theoretical results is given later in this paper.

For the case of continuous velocity profiles, the $O(\lambda^2)$ correction to the growth rate of the first helical mode is shown in figure 8 for various values of $(\theta_0)^{-1}$. Except for the highest value of $(\theta_0)^{-1}$, namely 40, the corrections are negative, indicating a stabilization of this first helical mode that enhances the role of the nominally axisymmetric mode as the most unstable mode. For $(\theta_0)^{-1} = 40$ (a value that requires (2.7) to be redefined), the correction becomes positive, which supports the inviscid result shown in figure 4 that indicates destabilization of the first helical mode. Yet

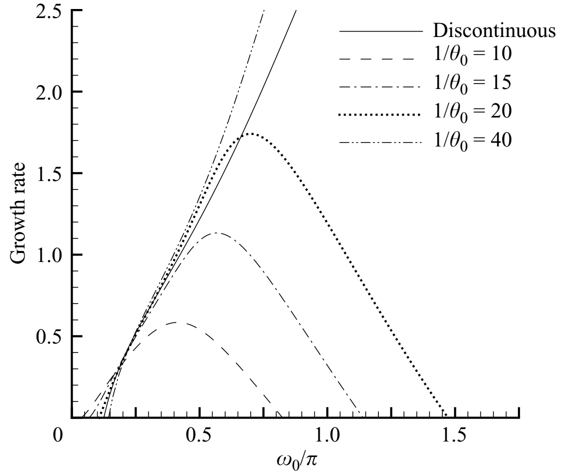

FIGURE 9. First helical mode growth rate versus ω_0/π from the tanh base flow model with $\lambda = 0.1$.

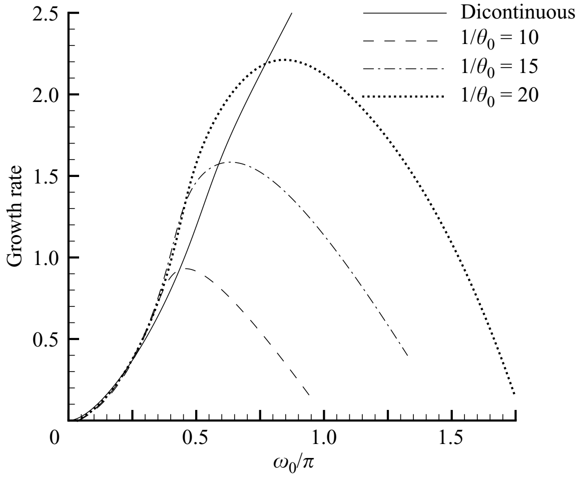

FIGURE 10. Axisymmetric mode growth rate versus ω_0/π from the tanh base flow model with $\lambda = 0.1$.

the nominally axisymmetric mode is still more unstable for the range of λ of interest to this analysis (say $\lambda < 1/4$ so that $\lambda^2 \lesssim 0.06$). Results given by de B. Alves (2006) show that the same trend is observed for the second helical mode ($m = 2$), with the destabilization appearing at a higher $(\theta_0)^{-1}$.

Comparison between discontinuous and continuous profiles was made in figure 3(*b*) for the free-jet growth rates for different values of $(\theta_0)^{-1}$. A similar comparison is now made in figure 9 for the jet in crossflow with $\lambda = 0.1$. For the higher values of $(\theta_0)^{-1}$, the maximum growth rates agree approximately with the values for discontinuous flow at the corresponding values of St. The value of St for maximum growth rate, however, can be determined only with the use of the continuous velocity profiles, as is clear in figure 9.

Results for the growth rate of the axisymmetric mode for the continuous base flow, shown in figure 10, are similar to those represented in figure 7, but are plotted

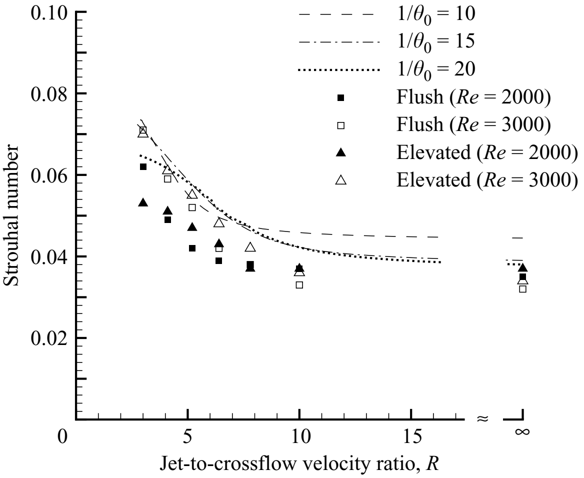

FIGURE 11. Comparison of predicted Strouhal number ($St_{\theta_0} \equiv f\theta_0/U_j$) associated with the most unstable axisymmetric mode disturbance (tanh base flow model) with experimentally measured values (from Part I) for different jet-to-crossflow velocity ratios $R \equiv 1/\lambda$ at two different jet Reynolds numbers, 2000 and 3000, for both flush and elevated nozzles used in the experiments.

for $\lambda = 0.1$ and for various values of $(\theta_0)^{-1}$. These are more easily compared to the behaviour of the first helical mode growth rate in figure 9. We conclude from such a comparison that the case with $m = 0$ is the more unstable mode when $\lambda = 0.1$ and $(\theta_0)^{-1} = 15$, since the maximum growth rate for the axisymmetric mode at these conditions is higher than that for the first helical mode. This is true for other values of $(\theta_0)^{-1}$ and for $\lambda < 0.25$ explored in this study (see de B. Alves 2006 for details). Thus we conclude that, within the framework of this linear stability analysis, the most unstable disturbance for $\lambda < 0.25$ ($R > 4$) corresponds to the nominally axisymmetric mode ($m = 0$).

We can now compare the predicted values for frequency of the most unstable disturbance to the experimental values given in figure 11 of Part 1. This comparison is shown in figure 11. Likewise, comparison of the theoretical growth rates for this most unstable disturbance ($m = 0$) to the experimentally measured values is given in figure 12. For both plots, the length scale used to non-dimensionalize frequency and growth rate is the local momentum thickness, θ_0, which in the case of the experiments was measured for different R (or λ) values at approximately $x = 0.2$ (or about 0.1 diameters above the jet exit plane).

We note that from table 2 of Part 1, measured values of $(\theta_0)^{-1}$ are close to 10 at $x = 0.2$ for the range of λ values relevant to the present study, in contrast to the value of 20 predicted by the estimation of Crighton & Gaster (1976) in (2.7) for the free jet. Nevertheless, the agreement between theory and experiments for the transverse jet in figure 11 is reasonable and, as expected for an inviscid stability analysis, the experimental data for the higher Reynolds number cases lie closer to the theoretical values. The significant increase in growth rate of the most unstable $m = 0$ disturbance with increasing λ (or decreasing R) that is predicted by the LSA for the continuous base flow is consistent with experimental findings.

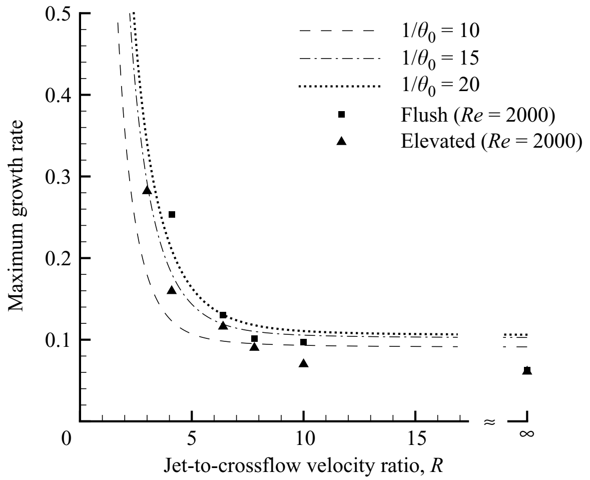

FIGURE 12. Comparison of predicted growth rates $-\mathrm{Im}[\alpha]\theta_0$ associated with the axisymmetric mode disturbances (tanh base flow model) with experimentally measured values (from Part 1), for different jet-to-crossflow velocity ratios $R \equiv 1/\lambda$ at a jet Reynolds number of 2000.

5. Discussion and conclusions

We have used discontinuous as well as continuous base flow models, based largely on a modified version of the solution of Coelho & Hunt (1989) for a transverse jet at large velocity ratios, combined with an inviscid three-dimensional stability analysis, to explore transverse-jet near-field shear-layer instability. For the continuous base flow analysis, both characteristic frequencies and growth rates associated with the axisymmetric mode increase as R decreases from infinity (i.e. as λ increases from zero), just as observed in experiments, as shown in figures 11 and 12. The discontinuous base flow analysis via a perturbation expansion approach suggests that an increasing crossflow (increasing λ or decreasing R) also increases the rate of growth of the first helical mode. That analysis further suggests that a subharmonic resonance associated with the first helical mode increases the destabilization brought about by increasing the crossflow. Nevertheless, as can be seen by a comparison of growth rates using the continuous base flow for the axisymmetric mode (figure 7) and first helical mode (figure 9), the dominant modes observed in experiments for $R > 4$ are probably associated primarily with a destabilized axisymmetric mode, and only to a minor degree with helical mode disturbances over the domain in x considered.

All theoretical results here are valid only for relatively large values of the velocity ratio, $R \gtrsim 4$, because this assumption is used in both the derivation of the base flow and in the linear stability analysis. The experimental results indicate that the nature of the instability changes significantly for $R < 3.5$, with instabilities becoming much stronger and exhibiting nonlinear behaviour much closer to the transverse jet orifice than for $R > 4$. Hence exploration of this flow regime would not be possible using the present type of linearized analysis, and clearly would have to be investigated with a different base flow model than that currently employed, i.e. one that represents greater jet distortion at large values of λ or lower values of R. The present model's consistency with experimentally observed instabilities, however, provides further evidence (in addition to experimental findings during low-level forcing) of the convective nature of the shear-layer instabilities in this higher R range. Any attempt to extend the analysis so as to include global instabilities, as discussed by Chomaz (2005), would require knowledge concerning the spatial evolution of the base flow.

Despite the robustness of the present findings, the present flow model nevertheless could be improved even in this $R > 4$ regime. This might be worthwhile if one wants to understand better the energy transfer mechanisms between the base flow and the disturbances that cause the increase in growth rate, such as the additional shear introduced by $\widehat{W}_1(r)$ (see figure 2*d*), as well as the 'mode shifting' along the jet that is observed in experiments (see Part 1). An altered analysis might also be used to confirm the conclusion from our continuous base flow model that the axisymmetric mode is the dominant instability, instead of the first helical mode as suggested by the potential flow analysis. Yet the consistency of the present results with experimental trends provides powerful additional evidence of the dominance of the convectively unstable axisymmetric mode, at least in the $R > 4$ regime.

The authors would like to acknowledge the financial support of CAPES/Brazil, the UCLA Graduate Division, the National Science Foundation under Grants CTS-0200999 and CTS-0457413 and NASA under Grant NCC-157.

REFERENCES

DE B. ALVES, L. S. 2006 Transverse jet shear-layer instabilities: Linear stability analysis and numerical simulations. PhD thesis, University of California at Los Angeles, Los Angeles, USA.

DE B. ALVES, L. S., KELLY, R. E. & KARAGOZIAN, A. R. 2007 Local stability analysis of an inviscid transverse jet. *J. Fluid Mech.* **581**, 401–418.

BATCHELOR, G. K. & GILL, A. E. 1962 Analysis of the stability of axisymmetric jets. *J. Fluid Mech.* **14**, 529–551.

BLOSSEY, P. N. & SCHMID, P. J. 2002 Global stability analysis of a jet in cross flow. *Bull. Am. Phys. Soc.* **47**, 10. 92.

CHOMAZ, J. M. 2005 Global instabilities in spatially developing flows: Non-normality and nonlinearity. *Annu. Rev. Fluid Mech.* **37**, 357–392.

COELHO, S. L. V. & HUNT, J. C. R. 1989 The dynamics of the near field of strong jets in cross flow. *J. Fluid Mech.* **200**, 95–120.

COHEN, J. & WYGNANSKI, I. 1987 The evolution of instabilities in the axisymmetric jet. Part 1. The linear growth of disturbances. *J. Fluid Mech.* **176**, 191–219.

CORKE, T. C. & KUSEK, S. M. 1993 Resonance in axisymmetric jets with controlled helical-mode input. *J. Fluid Mech.* **249**, 307–336.

CORTELEZZI, L. & KARAGOZIAN, A. R. 2001 On the formation of the counter-rotating vortex pair in transverse jets. *J. Fluid Mech.* **446**, 347–373.

CRIGHTON, D. G. & GASTER, M. 1976 Stability of slowly diverging jet flow. *J. Fluid Mech.* **77**, 397–413.

CROW, S. C. & CHAMPAGNE, F. M. 1971 Orderly structure in jet turbulence. *J. Fluid Mech.* **48**, 547–591.

FRIC, T. F. & ROSHKO, A 1994 Vortical structure in the wake of a transverse jet. *J. Fluid Mech.* **279**, 1–47.

HUERRE, P. & MONKEWITZ, P. A. 1990 Local and global instabilities in spatially developing flows. *Annu. Rev. Fluid Mech.* **22**, 473–537.

KELSO, R. & SMITS, A. 1995 Horseshoe vortex systems resulting from the interaction between a laminar boundary layer and a transverse jet. *Phys. Fluids* **7**, 153–158.

KELSO, R. M., LIM, T. T. & PERRY, A. E. 1996 An experimental study of round jets in cross flow. *J. Fluid Mech.* **306**, 111–144.

MEGERIAN, S., DAVITIAN, J., DE B. ALVES, L. S. & KARAGOZIAN, A. R. 2007 Transverse jet shear-layer instabilities. Part 1. Experimental studies. *J. Fluid Mech.* **593**, 93–129.

Michalke, A. 1984 Survey on jet instability theory. *Prog. Aerospace Sci.* **21**, 159–199.

Raman, G., Rice, E. J. & Reshotko, E. 1994 Mode spectra of natural disturbances in a circular jet and the effect of acoustic forcing. *Exps. Fluids* **17**, 415–426.

Schmid, P. 2007 Nonmodal stability theory. *Annu. Rev. Fluid Mech.* **39**, 129.

Wolfram, S. 1999 *The Mathematica Book*, 4th edn. Cambridge: Wolfram Media.

Yoda, M., Hesselink, L. & Mungal, M. G. 1992 The evolution and nature of large-scale structures in the turbulent jet. *Phys. Fluids* A **4**, 803–811.